Results in Engineering 27 (2025) 105631

Contents lists available at ScienceDirect

Results in Engineering

journal homepage: www.sciencedirect.com/journal/results-in-engineering

Frequency response of multi-degree-of-freedom hybrid offshore systems integrating wind and hydrokinetic turbines

Abdullah Kürşat DEMİR [a,*], Can Elmar BALAS [b]

[a] Graduate School of Natural and Applied Sciences, Gazi University, Ankara, Türkiye
[b] Sea and Aquatic Sciences Application and Research Center, Gazi University, Ankara, Türkiye

ARTICLE INFO

Keywords:
Blue energy
Combined offshore wind turbines
Multi-degree-of-freedom systems
Natural frequency analysis

ABSTRACT

Recent technological advancements have made marine energy a significant focus within renewable energy. Offshore wind turbines are usually installed on monopile foundations up to a certain depth. When these monopiles also support hydrokinetic turbines, they form combined hybrid systems. Natural frequency analysis is one of the most critical design criteria for these systems. Traditionally, offshore wind turbines have been analyzed using single-degree-of-freedom (SDOF) models. However, incorporating hydrokinetic turbines increases the system's complexity, requiring a multi-degree-of-freedom (MDOF) approach. This study performs a natural frequency analysis based on a two-degree-of-freedom model for such hybrid systems. Compared with a previous study, the analytical solution shows a difference of only 2.35 %, indicating strong consistency with the literature. Moreover, a 24.59 % decrease in the system's natural frequency is observed compared to the wind-only configuration, emphasizing the need for higher-order modeling in hybrid systems.

1. Introduction

The increasing global population, industrial development, and technological advancements have led to a growing demand for energy. Considering the environmental damage caused by petroleum-based solid fuels currently used in energy production, their negative impacts on ecological balance are evident. In contrast, renewable energy sources, derived from natural resources, have significantly lower adverse effects on ecological balance compared to these solid fuels. Blue energy, derived from seas and oceans, is highly important among renewable energy sources. Research has shown that seas and oceans hold more potential energy than the amount consumed globally [1]. Therefore, the key issue is how to optimally benefit from this potential.

Blue energy's components include offshore wind, hydrokinetic, tidal, and wave energy. These components are notable for having the lowest investment cost per MW among renewable energy sources [2]. Combined hybrid systems integrate multiple energy generators. The theoretical investigation of these systems has recently become a research subject [3–7]. Recent studies have expanded the research frontier in hybrid renewable energy systems by exploring advanced multi-energy coupling frameworks and intelligent control mechanisms. For instance [8], proposed a multi-energy inertia-based control strategy to enhance frequency and voltage stability in hybrid isolated systems [9] analyzed the feasibility of green hydrogen production from offshore hybrid energy resources, reinforcing the practical significance of such systems. Additionally, intelligent control frameworks using AI-based controllers have been explored for solar–biomass and wind–PV–battery systems, emphasizing real-time adaptation and predictive energy management [10–12]. These studies highlight current research priorities in hybrid system optimization and complement the present work, which aims to analyze coupled dynamic behavior in a multi-source offshore energy structure. The primary advantage of combined hybrid systems is their use of a shared support structure, thus providing cost and efficiency benefits.

Offshore wind turbines (OWTs) with monopile foundations are recommended for depths up to 50 m [13]. Hydrokinetic turbines, like offshore wind turbines, have monopile foundations [14]. This study presents the design of a combined hybrid system using both wind and hydrokinetic turbines on a monopile foundation.

Offshore wind energy plants are subjected to various repetitive loads, such as waves, wind, and currents, throughout their economic lifetime. Resonance occurs when the structure's natural frequency coincides with the frequency of these loads, leading to severe damage and potential collapse [15]. Therefore, natural frequency analysis is one of the most

* Corresponding author.
E-mail address: abdullahkursatdemir@gmail.com (A.K. DEMİR).

https://doi.org/10.1016/j.rineng.2025.105631
Received 22 April 2025; Received in revised form 2 June 2025; Accepted 3 June 2025
Available online 8 June 2025

critical design criteria for offshore wind turbines [16–20]. Natural frequency analysis is also important for combined hybrid systems during design. These analyses are performed in the literature using single-degree-of-freedom (SDOF) systems. However, with the addition of hydrokinetic turbines, these systems must be considered as multi-degree-of-freedom (MDOF) systems due to the increasing rotor diameters, power, and weight of the turbines. Multiple turbines' added weight and forces necessitate a multi-degree-of-freedom (MDOF) approach to achieve accurate frequency estimations.

Natural frequency analyses for combined hybrid systems in the literature have been conducted using finite element methods (FEM) [5,21]. However, depending on the project's scale, the finite element method's design and analysis processes can be time-consuming. This study uses analytical equations for combined hybrid systems and compares them with the literature. The analytical equations are consistent with the literature, allowing for rapid analysis of natural frequencies in the design of combined hybrid systems. The underlying mechanism of natural frequency analysis is explicitly presented in this study, guiding future combined hybrid system designs.

2. Methodology

The combined hybrid system considered in this study includes wind, wave, and hydrokinetic turbine rotor frequencies and operating ranges, as shown in Fig. 1.

As observed in Fig. 1, in the stiff-stiff design range, the structure's natural frequency is designed to be higher than both the wind (typically 1P; rotor frequency and 3P; blade shadowing frequency) and wave frequencies [15]. This design aims to prevent resonance between the wind and wave frequencies and the structure's natural frequency. The structure becomes very rigid, minimizing deformations under loads. The risk of resonance is minimized, and structural durability is maximized. However, stiff-stiff designs often result in heavier and more costly structures.

In soft-stiff design, the structure's natural frequency is designed to be higher than the wind frequencies but lower than the wave frequencies. This design reduces the likelihood of resonance with wind frequencies while making the structure more sensitive to wave frequencies. The structure is neither too rigid nor too flexible. Deformations are larger than stiff-stiff designs, but lighter and less costly structures can be built. The optimal design region lies in this area.

In soft-soft design, the structure's natural frequency is designed to be lower than both wind and wave frequencies. This design can lead to resonance, where the structure's natural frequency coincides with wind and wave frequencies, resulting in increased dynamic loads and significant deformations. This design region has the highest risk of resonance but results in lighter and more flexible structures.

As illustrated in Fig. 1, the soft–stiff design region for the hybrid system, which combines offshore wind and hydrokinetic turbines, is noticeably narrower than that of a conventional offshore wind turbine. This constraint becomes even more pronounced when a ±10 % safety margin is applied, as recommended by [22]. The narrowing is not primarily due to increased structural mass or coupling effects, but instead arises from the low rotational speed range of the hydrokinetic turbine. This is a direct consequence of the high density of water compared to air; hydrokinetic turbines can extract similar amounts of energy at significantly lower rotational speeds than wind turbines. As a result, their 1P and 3P excitation frequencies are tightly clustered and fall within a narrow frequency band. These frequencies significantly overlap with those of the wind turbine, reducing the available margin for placing natural frequencies outside excitation zones. Therefore, natural frequency analysis becomes particularly critical in the design of such combined hybrid systems.

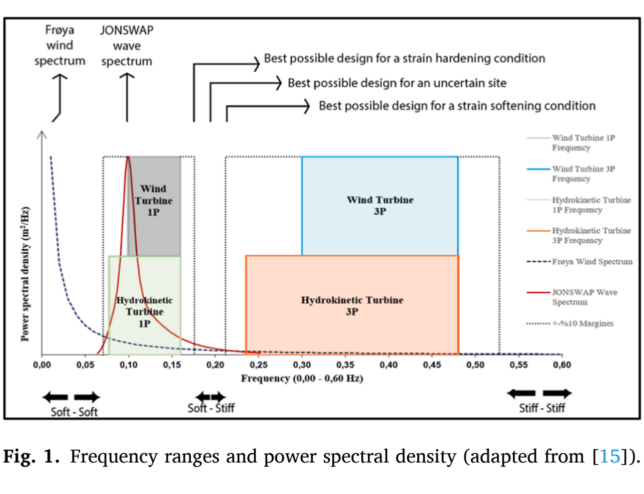

Fig. 1. Frequency ranges and power spectral density (adapted from [15]).

3. Principle equations

Natural frequency calculations for offshore wind turbines have traditionally been performed using single-degree-of-freedom (SDOF) systems [16,23]. However, combined hybrid systems, including hydrokinetic, wave, and wind turbines, should be considered second-degree-of-freedom (MDOF) systems (Fig. 2).

In Fig. 2, m_1 is the mass of the hydrokinetic turbine, m_2 is the mass of the wind turbine, F_2 is the force acting on the hydrokinetic turbine, F_1 is the force acting on the wind turbine, L_S is the vertical distance between the ground and the tower base, L_T is the length of the tower, L_C is the vertical distance between the tower base and the hydrokinetic turbine hub. This vertical offset is implicitly accounted for in the equivalent stiffness and effective mass calculations through the deformation mode shape and integration bounds applied in Castigliano's theorem. Thus, it contributes directly to the dynamic representation of the lower segment. $E_T I_T$ is the bending stiffness of the tower, and $E_P I_P$ is the bending stiffness of the monopile.

The basic equation for free harmonic motion for second-degree-of-freedom systems is given in Eq. 1.

$$[M]\{\ddot{x}\} + [k]\{x\} = 0 \tag{1}$$

Here, [M] is the mass matrix, $\{\ddot{x}\}$ is the acceleration vector, [k] is the stiffness matrix, and {x} is the displacement vector. Eq. (1) is expressed in its undamped form, as the combined effect of structural,

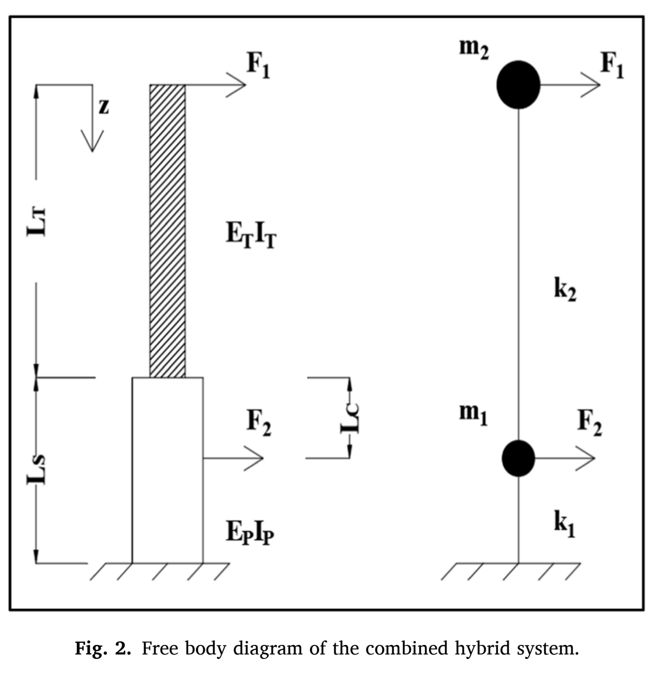

Fig. 2. Free body diagram of the combined hybrid system.

hydrodynamic, and aerodynamic damping on the natural frequency is considered relatively small. According to [16], the total damping ratio of the first vibration mode is typically between 1–4 % in the side-to-side direction and 2–8 % in the fore–and–aft direction for operational offshore wind turbines. Similarly, [23] reported that hydrodynamic damping has a negligible influence on modal frequencies in monopile-supported offshore structures. Therefore, damping is neglected in Eq. (1) to allow for a simplified yet sufficiently accurate estimation of the system's natural frequencies. It should be noted that this damping influence was not numerically verified within the scope of this study but was adopted from validated literature sources.

$$\{x\} = \{X\}e^{iwt} \tag{2}$$

With this transformation, Eq. 1 becomes Eq. 3.

$$\left([K] - w^2[M]\right)\{X\} = 0 \tag{3}$$

Eq. 3 is an eigenvalue problem. The determinant of the frequency-related part of the expression is taken and set to zero to obtain the angular frequency value (Eq. 4–5).

$$det\left([K] - w^2[M]\right) = 0 \tag{4}$$

$$w_{1,2}^2 = \frac{k_1m_2 + k_2m_2 + k_2m_1}{2m_1m_2} \pm \frac{\sqrt{(k_1m_2 + k_2m_2 + k_2m_1)^2 - 4m_1m_2k_1k_2}}{2m_1m_2} \tag{5}$$

Thus, the system's natural frequency is obtained as in Eq. 6.

$$f_{1,2} = \frac{w_{1,2}}{2\pi} \tag{6}$$

The required spring constants k_1 and k_2 in Eq. 5 are calculated using Eq. 7 and Eq. 8.

$$k_2 = \frac{F_2}{x_1 - x_2} \tag{7}$$

$$k_1 = \frac{F_1 + F_2}{x_2} \tag{8}$$

Here, x_1 is the displacement of the wind turbine, and x_2 is the displacement of the hydrokinetic turbine. The displacements x_1 and x_2 can be expressed using Castigliano's second theorem as in Eq. 9 and Eq. 10.

$$q_1 = \frac{\partial U}{\partial F_1} = x_1 \tag{9}$$

$$q_2 = \frac{\partial U}{\partial F_2} = x_2 \tag{10}$$

In Eqs. 9 and 10, q_i is the local deformation, and U is the strain energy. This energy is expressed by Eq. 11.

$$U = \int_0^{L_T+L_S} \frac{[M(z)]^2}{2EI(z)}dz \tag{11}$$

Here, M(z) is the moment value at the z, and EI(z) is the bending stiffness at the z. The moment values for each region can be written as in Eq. 12 to Eq. 14.

$$M(z) = F_1z \ (0 \leq z \leq L_T) \tag{12}$$

$$M(z) = F_1z \ (L_T \leq z \leq L_T + L_C) \tag{13}$$

$$M(z) = F_1z + F_2[z - L_T - L_C] \ (L_T + L_C \leq z \leq L_T + L_S) \tag{14}$$

By writing the strain energy for each deformation separately, the displacements at the turbine levels are obtained as in Eq. 15 and Eq. 16.

$$\begin{aligned} q_1 &= \frac{\partial U}{\partial F_1} = x_1 \\ &= \frac{F_1L_T^3}{3E_TI_T} + \frac{F_1}{E_PI_P}\left[\frac{(L_T+L_C)^3}{3} - \frac{L_T^3}{3}\right] \\ &\quad + \frac{1}{2E_PI_P}\left\{2(F_1+F_2)\left[\frac{(L_T+L_S)^3}{3} - \frac{(L_T+L_C)^3}{3}\right]\right. \\ &\quad \left. - 2F_2(L_T+L_C)\left[\frac{(L_T+L_S)^2}{2} - \frac{(L_T+L_C)^2}{2}\right]\right\} \end{aligned} \tag{15}$$

$$\begin{aligned} q_2 &= \frac{\partial U}{\partial F_2} = x_2 \\ &= \frac{1}{2E_PI_P}\left\{2(F_1+F_2)\left[\frac{(L_T+L_S)^3}{3}\right] - \frac{(L_T+L_C)^3}{3}\right. \\ &\quad - 2(F_1+2F_2)(L_T+L_C)\left[\frac{(L_T+L_S)^2}{2} - \frac{(L_T+L_C)^2}{2}\right] \\ &\quad \left. + 2F_2(L_T+L_C)^2[(L_T+L_S) - (L_T+L_C)]\right\} \end{aligned} \tag{16}$$

I_P is the moment of inertia of the monopile, and I_T is the moment of inertia of the tower. The moment of inertia of the monopile is calculated as in Eq. 17 [24].

$$I_P = \frac{1}{8}(D_P - t_P)^3 t_P\pi \tag{17}$$

Here, D_P is the diameter of the monopile, and t_P is the wall thickness of the monopile. This equation is valid for the entire pile since the diameter and wall thickness are constant along the pile. This equation is invalid for wind turbine towers because the tower diameter and wall thickness are different at the top and base. Typically, the tower diameter and wall thickness are smaller at the top and increase towards the base, providing stability and cost savings. Therefore, the moment of inertia varies along the tower [24] proposed Eq. 18 for the moment of inertia of the tower.

$$I_T = \frac{1}{16}\left({D_b}^3 + {D_t}^3\right)t_T\pi \tag{18}$$

Here, D_b is the tower's diameter at the base, Dt is the tower's diameter at the top, and t_T is the average wall thickness of the tower. The average thickness of the tower is determined by Eq. 19 [24].

$$t_T = \frac{m_T}{\rho_T L_T D_T \pi} \tag{19}$$

Here, m_T is the tower's weight, ρ_T is the density of the tower material, L_T is the tower's length, and D_T is the average diameter of the tower. The average diameter of the tower is calculated by Eq. 20 [24].

$$D_T = \frac{1}{2}(D_b + D_t) \tag{20}$$

All calculations up to this point are for the fixed-base solution of the combined hybrid system's support structure. However, when the soil effect is considered, calculations are made by considering the geometric condition proposed by [20]. The effect of the soil on the natural frequency is considered using a simplified three springs (Fig. 3) at the ground level [16,20,25].

In Fig. 3, y_0 is the displacement at the ground level, y_1 is the displacement at the hydrokinetic turbine level, y_2 is the displacement at the wind turbine level, ψ_0 is the rotation at the ground level, ψ_1 is the rotation at the hydrokinetic turbine level, K_R is the rotational stiffness, K_L is the lateral stiffness, and K_{LR} is the cross-coupling stiffness. Considering the geometric conditions, Eq. 21 and Eq. 22 can be written.

The displacement and rotation values at the ground level are calculated using Eq. 23 [20].

$$y_1 = y_0 + (L_S - L_C)\sin\psi_0 + \frac{\partial U}{\partial F_2} \tag{21}$$

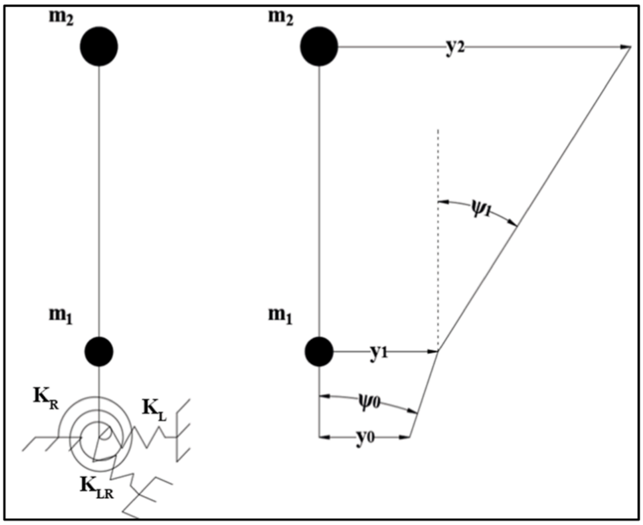

Fig. 3. Deformation mode of the combined hybrid system (adapted from [20]).

$$y_2 = y_1 + (L_T + L_C)\sin\psi_1 + \frac{\partial U}{\partial F_1} \tag{22}$$

$$\begin{Bmatrix} y_0 \\ \psi_0 \end{Bmatrix} = \begin{bmatrix} \delta_L & \delta_{LR} \\ \delta_{LR} & \delta_R \end{bmatrix} \begin{Bmatrix} F_0 \\ M_0 \end{Bmatrix} \tag{23}$$

Here, F_0 is the horizontal force at the ground level, M_0 is the moment at the ground level, y_0 is the lateral displacement at the ground level, and ψ_0 is the rotation at the ground level. These values can be expressed explicitly using Eq. 24 and Eq. 25.

$$y_0 = \delta_L F_0 + \delta_{LR} M_0 \tag{24}$$

$$\psi_0 = \delta_{LR} F_0 + \delta_R M_0 \tag{25}$$

Here, δ_L is the horizontal flexibility, δ_R is the rotational flexibility, and δ_{LR} is the coupling flexibility. According to [26], these coefficients vary depending on the pile type and soil. These coefficients are given in Eqn. 26 for non-cohesive soils and slender piles.

$$\begin{Bmatrix} y_0 \\ \psi_0 \end{Bmatrix} = \begin{bmatrix} \dfrac{2,40}{n_h^{3/5}(E_P I_P)^{2/5}} & \dfrac{1,60}{n_h^{2/5}(E_P I_P)^{3/5}} \\ \dfrac{1,60}{n_h^{2/5}(E_P I_P)^{3/5}} & \dfrac{1,74}{n_h^{1/5}(E_P I_P)^{4/5}} \end{bmatrix} \begin{Bmatrix} F_0 \\ M_0 \end{Bmatrix} \tag{26}$$

For non-cohesive soils with rigid piles, Eq. 27 is used [26].

$$\begin{Bmatrix} y_0 \\ \psi_0 \end{Bmatrix} = \begin{bmatrix} \dfrac{18}{L_P^2 n_h} & \dfrac{24}{L_P^3 n_h} \\ \dfrac{24}{L_P^3 n_h} & \dfrac{36}{L_P^4 n_h} \end{bmatrix} \begin{Bmatrix} F_0 \\ M_0 \end{Bmatrix} \tag{27}$$

Here, n_h is the coefficient of the subgrade reaction, and L_P is the embedded length of the monopile.

The rigid or slender of the pile in cohesionless soils is determined using Eqs. 28 and 29.

$$L_P > 4,0\left(\frac{E_P I_P}{n_h}\right)^{\frac{1}{5}} \tag{28}$$

The pile is considered slender if the embedded pile length satisfies Eq. 28. If it satisfies Eq. 29, the pile is defined as a rigid pile [26].

$$L_P < 2,0\left(\frac{E_P I_P}{n_h}\right)^{\frac{1}{5}} \tag{29}$$

The coefficient of the subgrade reaction is provided in Table 1 by [27].

The coefficients are provided in Eq. 30 for cohesive soils and slender piles.

$$\begin{Bmatrix} y_0 \\ \psi_0 \end{Bmatrix} = \begin{bmatrix} \dfrac{2\beta}{k_h D_P} & \dfrac{2\beta^2}{k_h D_P} \\ \dfrac{2\beta^2}{k_h D_P} & \dfrac{4\beta^3}{k_h D_P} \end{bmatrix} \begin{Bmatrix} F_0 \\ M_0 \end{Bmatrix} \tag{30}$$

The coefficients are given in Eq. 31 for cohesive soils and rigid piles.

$$\begin{Bmatrix} y_0 \\ \psi_0 \end{Bmatrix} = \begin{bmatrix} \dfrac{4}{k_h D_P L_P} & \dfrac{6}{k_h D_P {L_P}^2} \\ \dfrac{6}{k_h D_P {L_P}^2} & \dfrac{12}{k_h D_P {L_P}^3} \end{bmatrix} \begin{Bmatrix} F_0 \\ M_0 \end{Bmatrix} \tag{31}$$

Here, k_h is the modulus of the subgrade reaction, and β is the slenderness parameter. This parameter is constant for cohesive soils and is given in Eq. 32 [28].

$$k_h = \frac{0,65}{D_P}\sqrt[12]{\frac{E D_P^4}{E_P I_P}}\left(\frac{E}{1-\nu_s^2}\right) \tag{32}$$

Here, E is the soil's modulus of elasticity, and ν is the Poisson's ratio of the soil. In cohesive soils, this value remains constant along the depth. However, it increases linearly with depth in non-cohesive soils, as expressed in Eq. 33.

$$k_h = n_h \frac{z}{D_P} \tag{33}$$

The slenderness parameter β is given by Eq. 34 [26].

$$\beta = \sqrt[4]{\frac{k_h D_P}{4 E_P I_P}} \tag{34}$$

In non-cohesive soils, the pile is rigid when Eq. 35 is satisfied.

$$L_P < 1,5\left(\frac{4 E_P I_P}{k_h D_P}\right)^{\frac{1}{4}} \tag{35}$$

In non-cohesive soils, the boundary condition for the slenderness of the pile is given by Eq. 36.

$$L_P > 2,5\left(\frac{4 E_P I_P}{k_h D_P}\right)^{\frac{1}{4}} \tag{36}$$

When Eqs. 21 and 22 are examined, the only unknown variable is observed to be ψ_1. The system should be transformed into an equivalent system that can produce the same displacements, considering the effect of the soil on determining this angle. For this purpose, the moment of inertia of the section representing the k_1 spring can be defined as I_{e1}, and the moment of inertia of the section representing the k_2 spring can be expressed as I_{e2} (Fig. 4).

Under the same applied force, the deformations of the equivalent combined system and the normal combined system must be equal, and to achieve this, the overall deformation of the equivalent system must be calculated. The system is analyzed in two parts, as expressed in Eqs. 37

Table 1
Coefficient of the subgrade reaction [27].

Relative Density	n_h (kN/m^3)		
	Loose	Medium	Dense
For soils above the groundwater level	2424	7272	19,393
For soils below the groundwater level	1385	4848	11,774

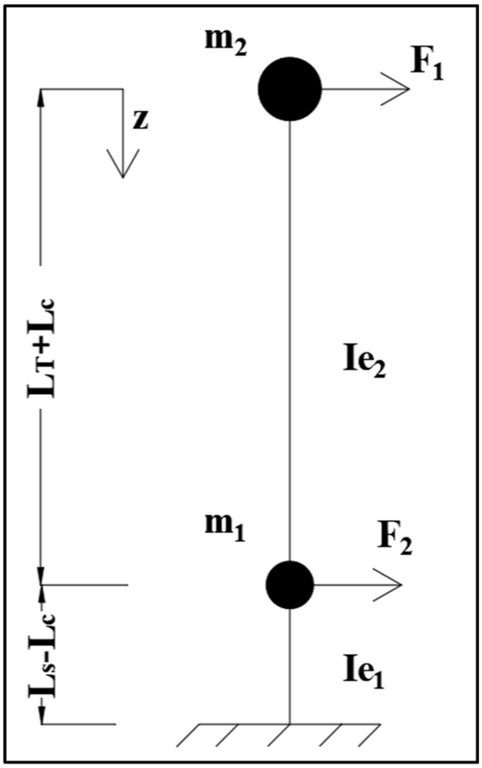

Fig. 4. Equivalent combined hybrid system with fixed support.

and 38.

$$M(z) = F_1 z \ (0 \le z \le L_T) \tag{37}$$

$$M(z) = F_1 z + F_2[z - L_T - L_C] \ (L_T + L_C \le z \le L_T + L_S) \tag{38}$$

The generalized deformation energy for each section can be expressed as in Equations 39 and 40.

$$U_1 = \int_0^{L_T+L_C} \frac{(F_1 z)^2}{2EI_{e2}} dz = \frac{F_1^2 (L_T + L_C)^3}{6EI_{e2}} \tag{39}$$

$$U_2 = \int_{L_T+L_C}^{L_T+L_S} \frac{(F_1 z + F_2[z - (L_T + L_C)])^2}{2EI_{e1}} dz$$

$$\begin{aligned} U_2 = {} & \frac{1}{2EI_{e1}} \left\{ (F_1 + F_2)^2 \left[\frac{(L_T + L_S)^3}{3} - \frac{(L_T + L_C)^3}{3} \right] \right\} - \\ & -2(F_1 + F_2)F_2(L_T + L_C)\left[\frac{(L_T + L_S)^2}{2} - \frac{(L_T + L_C)^2}{2} \right] + \\ & F_2^2 (L_T + L_C)^2 [(L_T + L_S) - (L_T + L_C)] \end{aligned} \tag{40}$$

EI_{e1} is the bending stiffness of the first section, and EI_{e2} is the bending stiffness of the second section. The total deformation energy is obtained by summing Eqs. 39 and 40. By taking the derivative of the total deformation energy for the force F_2, the deformation at the hydrokinetic turbine point in the equivalent system is determined (Eq. 41).

$$\frac{\partial U}{\partial F_2} = \frac{1}{2EI_{e1}} \left\{ \begin{array}{l} (F_1 + F_2)^2 \left[\frac{(L_T + L_S)^3}{3} - \frac{(L_T + L_C)^3}{3} \right] - \\ -2(F_1 + F_2)F_2(L_T + L_C)\left[\frac{(L_T + L_S)^2}{2} - \frac{(L_T + L_C)^2}{2} \right] + \\ F_2^2 (L_T + L_C)^2 [(L_T + L_S) - (L_T + L_C)] \end{array} \right\} \tag{41}$$

If Eq. 41 equals Eq. 21, the displacement at the hydrokinetic turbine point in the combined hybrid system with fixed support y_1 equals the displacement considering the soil effect (Eq. 42).

$$y_0 + (L_S - L_C)\sin\psi_0 + \frac{\partial U}{\partial F_2} = \frac{1}{2EI_{e1}} \left\{ \begin{array}{l} (F_1 + F_2)^2 \\ \left[\frac{(L_T + L_S)^3}{3} - \frac{(L_T + L_C)^3}{3} \right] - 2(F_1 + F_2)F_2(L_T + L_C) \\ \left[\frac{(L_T + L_S)^2}{2} - \frac{(L_T + L_C)^2}{2} \right] + F_2^2 (L_T + L_C)^2 \\ (L_T + L_S) - (L_T + L_C) \end{array} \right\} \tag{42}$$

From Eq. 42, the value of EI_{e1} is determined using Eq. 43.

$$EI_{e1} = \frac{1}{2\left(y_0 + (L_S - L_C)\sin\psi_0 + \frac{\partial U}{\partial F_2} \right)} \left\{ \begin{array}{l} 2(F_1 + F_2) \\ \left[\frac{(L_T + L_S)^3}{3} - \frac{(L_T + L_C)^3}{3} \right] - 2(F_1 + F_2)F_2(L_T + L_C) \\ \left[\frac{(L_T + L_S)^2}{2} - \frac{(L_T + L_C)^2}{2} \right] + 2F_2 (L_T + L_C)^2 \\ (L_T + L_S) - (L_T + L_C) \end{array} \right\} \tag{43}$$

The values of ψ_0 and ψ_1 are updated as expressed in Eqs. 44 and 45.

$$y_0 = \delta_L (F_1 + F_2) + \delta_{LR} [F_1 (L_T + L_S) + F_2 (L_S - L_C)] \tag{44}$$

$$\psi_0 = \delta_{LR}(F_1 + F_2) + \delta_R[F_1(L_T + L_S) + F_2(L_S - L_C)] \tag{45}$$

Thus, by substituting these values into Eq. 43, the bending stiffness of the first section is obtained. The primary purpose of determining this value is to solve for the unknown ψ_1. The moment-displacement relationship for the first region is expressed in Eq. 46.

$$EI_{e1}\frac{d^2 w_1}{dz^2} = F_1 z + F_2[z - (L_T + L_C)] \tag{46}$$

Here, w_1 is the deformation profile in the first region. The rotation profile is obtained by integrating Eq. 46, as expressed in Eq. 47.

$$\frac{dw_1}{dz} = \frac{1}{EI_{e1}}\left\{F_1\frac{z^2}{2} + F_2\left[\frac{z^2}{2} - (L_T + L_C)z\right]\right\} + C_1 \tag{47}$$

Here, C_1 is the integration constant. Since the rotation value at the ground level, ψ_0, is known as the boundary condition, substituting it into Eq. 47 results in Eqs. 48 and 49.

$$\begin{aligned} &z = L_T + L_S;\ \frac{dw_1}{dz} = -\psi_0 \\ &-\psi_0 = \frac{1}{EI_{e1}}\left\{\begin{aligned} &F_1\frac{(L_T + L_S)^2}{2} + F_2\left[\frac{(L_T + L_S)^2}{2} - \right. \\ &\left.(L_T + L_C)(L_T + L_S)\right]\} + C_1 \end{aligned}\right\} \end{aligned} \tag{48}$$

$$C_1 = -\psi_0 - \frac{1}{EI_{e1}}\left\{\left\{F_1\frac{(L_T + L_S)^2}{2} + F_2\left[\frac{(L_T + L_S)^2}{2} - (L_T + L_C)(L_T + L_S)\right]\right\}\right. \tag{49}$$

Therefore, the general rotation profile in the first region is expressed as in Eq. 50.

$$\begin{aligned} \frac{dw_1}{dz} &= \frac{1}{EI_{e1}}\left\{F_1\frac{z^2}{2} + F_2\left[\frac{z^2}{2} - (L_T + L_C)z\right]\right\} - \\ \psi_0 &- \frac{1}{EI_{e1}}\left\{F_1\frac{(L_T + L_S)^2}{2} + F_2\left[\frac{(L_T + L_S)^2}{2} - (L_T + L_C)(L_T + L_S)\right]\right\} \end{aligned} \tag{50}$$

By substituting the hydrokinetic turbine's position into Eq. 50, Eq. 51 is obtained, which represents the rotational value, ψ_1, at the hydrokinetic turbine level.

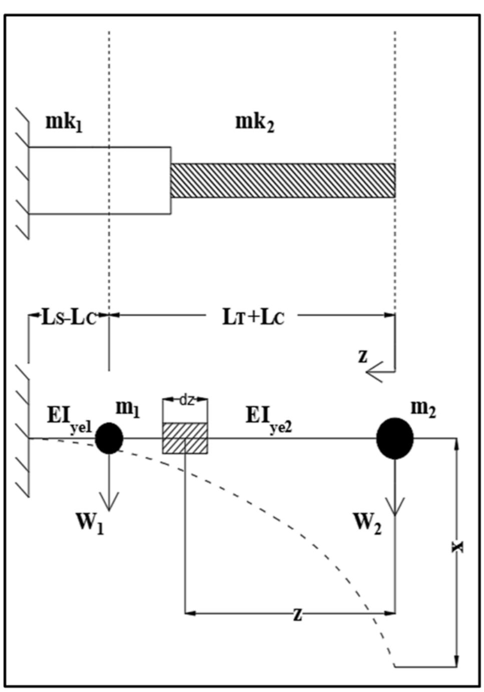

Fig. 5. Representation of the masses of beams.

$$\begin{aligned} \frac{dw_1}{dz} &= \frac{1}{EI_{e1}}\left\{F_1\frac{z^2}{2} + F_2\left[\frac{z^2}{2} - (L_T + L_C)z\right]\right\} - \\ \psi_0 &- \frac{1}{EI_{e1}}\left\{F_1\frac{(L_T + L_S)^2}{2} + F_2\left[\frac{(L_T + L_S)^2}{2} - (L_T + L_C)(L_T + L_S)\right]\right. \end{aligned} \tag{51}$$

By substituting the hydrokinetic turbine's position into Eq. 52, Eq. 51 is obtained, which represents the rotation value, ψ_1, at the hydrokinetic turbine level.

$$\begin{aligned} \psi_1 &= \frac{1}{EI_{e1}}\left\{F_1\frac{(L_T + L_C)^2}{2} + F_2\left[\frac{(L_T + L_C)^2}{2} - \right](L_T + L_C)(L_T + L_C)\right\} \\ -\psi_0 &- \frac{1}{EI_{e1}}\left\{F_1\frac{(L_T + L_s)^2}{2} + F_2\left[\frac{(L_T + L_S)^2}{2} - (L_T + L_C)(L_T + L_S)\right]\right\} \end{aligned} \tag{52}$$

In Eq. 52, the only unknown term is the bending stiffness, EI_{e1}.

4. Effective mass

For Eq. 4 to be valid, the fixed-support solution of the combined hybrid system is required; therefore, the system has been modified to account for soil effects. In the natural frequency analysis, the masses of the turbines and the tower must be included. In the natural frequency analysis of single-degree-of-freedom systems, the effective mass of the tower is considered using specific coefficients found in the literature [16,20,25,29] states that these coefficients are related to the deformation mode. Therefore, obtaining the displacement curves for both regions is necessary to calculate the effective masses in the combined hybrid system. In previous studies, the effective mass factors are commonly assumed as constant coefficients; for instance, [16] uses 33/140≈0.236, and [20] adopts 0.228. However, these empirical constants vary significantly across the literature and are sensitive to assumed boundary conditions, structural configurations, and modal characteristics. A non-constant, system-dependent effective mass factor is adopted in the present study. This factor is later defined based on mode shape integration, allowing it to represent better the dynamic response of the combined hybrid system under site-specific and structural variations. Considering soil effects, the system has been modeled as shown in Fig. 5.

In Fig. 5, EI_{ye1} is the bending stiffness of the first section with a fixed support, and EI_{ye2} is the bending stiffness of the second section with a fixed support. Additionally, m_1 is the mass of the hydrokinetic turbine, and m_2 is the mass of the wind turbine. The value of EI_{ye1} is equivalent to EI_{e1} in physical and mathematical implications. However, since the boundary conditions will be written differently during the derivation of the equation, different notations are used to avoid any conceptual confusion. The relationship between moment and rotation for the first region is expressed in Eq. 53.

$$\begin{aligned} EI_{ye1}\frac{d^2 w_1}{dz^2} &= M \\ EI_{ye1}\frac{d^2 w_1}{dz^2} &= F_1 z + F_2[z - (L_T + L_C)] \end{aligned} \tag{53}$$

While beam theory–based models can effectively capture structural bending deformations and distributed mass characteristics, they are often used in the literature to derive approximate analytical solutions that ultimately reduce the system to a single degree of freedom. For instance, the model in [16] employs beam theory for deformation estimation but does not explicitly resolve multiple dynamic degrees of freedom in coupled hybrid systems.

In contrast, the present study develops a two-degree-of-freedom (2DOF) formulation to capture the coupled dynamics between the wind and hydrokinetic turbines. The effective mass coefficients are not assumed to be fixed empirical values. They are derived analytically based on the deformation mode shapes of the system, enabling the mass distribution and stiffness to be included in a mode-specific manner. This ensures that the physical interaction between turbine subsystems is dynamically represented, providing enhanced fidelity in natural frequency predictions for hybrid offshore configurations.

Although beam theory provides an efficient framework for evaluating structural deformation under simplified loading and boundary conditions, it typically assumes uniform material properties and idealized supports. As such, classical beam models may not readily adapt to hybrid energy systems involving multiple dynamic subsystems, variable stiffness distributions, or soil–structure interactions. In contrast, the proposed MDOF formulation offers analytical flexibility to incorporate such interactions explicitly. This generalization makes it suitable not only for monopile-based fixed structures but also for potential extensions to floating offshore wind platforms or hybrid foundations with embedded coupling effects. Thus, the added complexity is justified by the model's broader applicability and improved accuracy.

In Eq. (53), w_1 represents the deformation profile in the first region. The rotation profile is obtained by integrating Eq. 53, as expressed in Eq. 54.

$$\frac{dw_1}{dz} = \frac{1}{EI_{ye1}}\left\{F_1\frac{z^2}{2} + F_2\left[\frac{z^2}{2} - (L_T + L_C)z\right]\right\} + C_2 \tag{54}$$

e:inline-figure))"^?^(1)[?tal = 1] > In Eq. (54), C_2 is the integration constant. The boundary condition for the fixed support with no rotation at the ground level is known. The integration constant can be determined by substituting this into Eq. 54 (Eq. 55).

$$\begin{gathered} z = L_T + L_S;\ \frac{dw_1}{dz} = 0 \\ 0 = \frac{1}{EI_{ye1}}\left\{F_1\frac{(L_T+L_S)^2}{2} + F_2\left[\frac{(L_T+L_S)^2}{2} - (L_T+L_C)(L_T+L_S)\right]\right\} + C_2 \\ C_2 = -\frac{1}{EI_{ye1}}\left\{F_1\frac{(L_T+L_S)^2}{2} + F_2\left[\frac{(L_T+L_S)^2}{2} - (L_T+L_C)(L_T+L_S)\right]\right\} \end{gathered} \tag{55}$$

The rotation profile is obtained by substituting the integration constant, as expressed in Eq. 56.

$$\begin{aligned} \frac{dw_1}{dz} = {} & \frac{1}{EI_{ye1}}\left\{F_1\frac{z^2}{2} + F_2\left[\frac{z^2}{2} - (L_T+L_C)z\right]\right\} - \\ & \frac{1}{EI_{ye1}}\left\{F_1\frac{(L_T+L_S)^2}{2} + F_2\left[\frac{(L_T+L_S)^2}{2} - (L_T+L_C)(L_T+L_S)\right]\right\} \end{aligned} \tag{56}$$

The deformation profile is obtained by integrating Eq. 56, as expressed in Eq. 57.

$$\begin{aligned} w_1 = {} & \frac{1}{EI_{ye1}}\left\{F_1\frac{z^3}{6} + F_2\left[\frac{z^3}{6} - (L_T+L_C)\frac{z^2}{2}\right]\right\} \\ & \frac{1}{EI_{ye1}}\left\{F_1\frac{(L_T+L_S)^2}{2} + F_2\left[\frac{(L_T+L_S)^2}{2} - (L_T+L_C)(L_T+L_S)\right]\right\}Z + C_3 \end{aligned} \tag{57}$$

Here, C_3 is the integration constant. As a boundary condition, in the case of a fixed support, no deformation occurs at the support. Thus, Eq. 58 is written to determine the integration constant.

$$\begin{gathered} z = L_T + L_S; w_1 = 0 \\ 0 = \frac{1}{EI_{ye1}}\left\{F_1\frac{(L_T+L_S)^3}{6} + F_2\left[\frac{(L_T+L_S)^3}{6} - (L_T+L_C)\frac{(L_T+L_S)^2}{2}\right]\right\} - \\ \frac{1}{EI_{ye1}}\left\{F_1\frac{(L_T+L_S)^2}{2} + F_2\left[\frac{(L_T+L_S)^2}{2} - (L_T+L_C)(L_T+L_S)\right]\right\}(L_T+L_S) + C_3 \end{gathered} \tag{58}$$

Therefore, the integration constant C_3 is obtained as expressed in Eq. 59.

$$\begin{aligned} C_3 = {} & -\frac{1}{EI_{ye1}}\left\{F_1\frac{(L_T+L_S)^3}{6} + F_2\left[\frac{(L_T+L_S)^3}{6} - (L_T+L_C)\frac{(L_T+L_S)^2}{2}\right]\right\} - \\ & \frac{1}{EI_{e1}}\left\{F_1\frac{(L_T+L_S)^2}{2} + F_2\left[\frac{(L_T+L_S)^2}{2} - (L_T+L_C)(L_T+L_S)\right]\right\}(L_T+L_S) \end{aligned} \tag{59}$$

Thus, the deformation profile for the first section is obtained as expressed in Eq. 60.

$$\begin{aligned} w_1 = {} & \frac{1}{EI_{ye1}}\left\{F_1\frac{z^3}{6} + F_2\left[\frac{z^3}{6} - (L_T+L_C)\frac{z^2}{2}\right]\right\} - \\ & \frac{1}{EI_{ye1}}\left\{F_1\frac{(L_T+L_S)^2}{2} + F_2\left[\frac{(L_T+L_S)^2}{2} - (L_T+L_C)(L_T+L_S)\right]\right\}z - \\ & \frac{1}{EI_{ye1}}\left\{F_1\frac{(L_T+L_S)^3}{6} + F_2\left[\frac{(L_T+L_S)^3}{6}\right] - (L_T+L_C)\frac{(L_T+L_S)^2}{2}\right\} + \\ & \frac{1}{EI_{ye1}}\left\{F_1\frac{(L_T+L_S)^2}{2} + F_2\left[\frac{(L_T+L_S)^2}{2} - (L_T+L_C)(L_T+L_S)\right]\right\}(L_T+L_S) \end{aligned} \tag{60}$$

The bending stiffness in the first region, EI_{ye1}, is determined using the known displacement value at the hydrokinetic turbine point (Eq. 61).

$$\begin{aligned} & z = L_T + L_C; w_1 = y_1 \\ y_1 = {} & \frac{1}{EI_{ye1}}\left\{F_1\frac{(L_T+L_C)^3}{6} + F_2\left[\frac{(L_T+L_C)^3}{6} - (L_T+L_C)\frac{(L_T+L_C)^2}{2}\right]\right\} - \\ & \frac{1}{EI_{ye1}}\left\{F_1\frac{(L_T+L_S)^2}{2} + F_2\left[\frac{(L_T+L_S)^2}{2} - (L_T+L_C)(L_T+L_S)\right]\right\}(L_T+L_C) - \\ & \frac{1}{EI_{ye1}}\left\{F_1\frac{(L_T+L_S)^3}{6} + F_2\left[\frac{(L_T+L_S)^3}{6} - (L_T+L_C)\frac{(L_T+L_S)^2}{2}\right]\right\} + \\ & \frac{1}{EI_{ye1}}\left\{F_1\frac{(L_T+L_S)^2}{2} + F_2\left[\frac{(L_T+L_S)^2}{2} - (L_T+L_C)(L_T+L_S)\right]\right\}(L_T+L_S) \end{aligned} \tag{61}$$

Therefore, the bending stiffness for the first region, EI_{ye1}, is calculated using Equation 62.

$$\begin{aligned} EI_{ye1} = {} & \frac{1}{y_1}\left\{F_1\frac{(L_T+L_C)^3}{6} + F_2\left[\frac{(L_T+L_C)^3}{6} - (L_T+L_C)\frac{(L_T+L_C)^2}{2}\right]\right\} - \\ & \frac{1}{y_1}\left\{F_1\frac{(L_T+L_S)^2}{2} + F_2\left[\frac{(L_T+L_S)^2}{2} - (L_T+L_C)(L_T+L_S)\right]\right\}(L_T+L_C) - \\ & \frac{1}{y_1}\left\{F_1\frac{(L_T+L_S)^3}{6} + F_2\left[\frac{(L_T+L_S)^3}{6} - (L_T+L_C)\frac{(L_T+L_C)^2}{2}\right]\right\} + \\ & \frac{1}{y_1}\left\{F_1\frac{(L_T+L_S)^2}{2} + F_2\left[\frac{(L_T+L_S)^2}{2} - (L_T+L_C)(L_T+L_S)\right]\right\}(L_T+L_S) \end{aligned} \tag{62}$$

In the first region, the maximum velocity occurs at the point of maximum deformation, where the force is applied (Eq. 63).

$$w_{1,m} = y_1 \tag{63}$$

Deformations and velocities are directly related to each other. Therefore, the velocity profile can be expressed as in Eq. 64.

$$v = \frac{w_1}{w_{1,m}}v_{max} \tag{64}$$

Here, v is the velocity at any given position, and v_{max} is the maximum velocity. Accordingly, the kinetic energy of a differential element in the first region, dT, can be expressed as in Eq. 65.

$$dT = \frac{1}{2}\rho A dz\left(\frac{w_1}{w_{1,m}}v_{max}\right)^2 \tag{65}$$

Here, ρ is the material density, A is the cross-sectional area, and dz is the length of the differential element. Consequently, the kinetic energy of the first section is determined using Eqs. 66 and 67.

$$T_1 = \frac{1}{2}\int_{L_T+L_C}^{L_T+L_S} \rho A\left(\frac{w_1}{w_{1,m}}v_{max}\right)^2 dz \tag{66}$$

$$T_1 = \frac{1}{2}\rho A {v_{max}}^2 \frac{1}{{w_{1,m}}^2}\int_{L_T+L_C}^{L_T+L_S} (w_1)^2 dz \tag{67}$$

By dividing the numerator and denominator by the difference between the upper and lower integral limits, Eq. 67 transforms into Eq. 68.

$$T_1 = \frac{1}{2}m_{k1}\frac{{v_{max}}^2}{(L_S - L_C)}\frac{1}{{w_{1,m}}^2}\int_{L_T+L_C}^{L_T+L_S} (w_1)^2 dz \tag{68}$$

Here, m_{k1} represents the mass of the first section and is given by Eq. 69.

$$m_{k1} = \rho A(L_S - L_C) \tag{69}$$

The coefficient for the effective mass is calculated using the expression in Eq. 70.

$$m_{eff1} = \left[\frac{1}{(L_S - L_C)}\frac{1}{{y_1}^2}\int_{L_T+L_C}^{L_T+L_S} (w_1)^2 dz\right] \tag{70}$$

Here, m_{eff1} is the effective mass coefficient for the first region. Consequently, in the natural frequency analysis, the mass in the first region, m_1, can be expressed using Eq. 71.

$$\begin{aligned} &z = L_T + L_C;\; w_2 = y_1 \\ &y_1 = \frac{1}{EI_{ye2}}\left\{F_1\frac{(L_T+L_c)^3}{6}\right\} + (\psi_0 - \psi_1)(L_T+L_c) - \frac{1}{EI_{ye2}}\left\{F_1\frac{(L_T+L_c)^2}{2}\right\}(L_T+L_c) + C_5 \\ &C_5 = y_1 - \frac{1}{EI_{ye2}}\left\{F_1\frac{(L_T+L_c)^3}{6}\right\} - (\psi_0 - \psi_1)(L_T+L_c) + \frac{1}{EI_{ye2}}\left\{F_1\frac{(L_T+L_c)^2}{2}\right\}(L_T+L_c) \end{aligned} \tag{79}$$

$$m_1 = m_{HYD} + m_{eff1} \times m_{k1} \tag{71}$$

Similarly, applying the same procedures to the second section can determine the value of EI_{ye2} and the elastic curve equation. The second section's relationship between moment and rotation can be expressed as in Eq. 72.

$$\begin{aligned} EI_{ye2}\frac{d^2w_2}{dz^2} &= M \\ EI_{ye2}\frac{d^2w_2}{dz^2} &= F_1 z \end{aligned} \tag{72}$$

In Eq. (72), w_2 is the deformation profile in the second section. The rotation profile is obtained by integrating Eq. 72, as expressed in Eq. 73.

$$\frac{dw_2}{dz} = \frac{1}{EI_{ye2}}\left\{F_1\frac{z^2}{2}\right\} + C_4 \tag{73}$$

Here, C_4 is the integration constant. Since the rotational value of the hydrokinetic turbine relative to the ground level is known as a boundary condition, substituting Eq. 74 into Eq. 75 results in Eq. 76.

$$z = L_T + L_C;\; \frac{dw_2}{dz} = \psi_0 - \psi_1 \tag{74}$$

$$\psi_0 - \psi_1 = \frac{1}{EI_{ye2}}\left\{F_1\frac{(L_T+L_c)^2}{2}\right\} + C_4 \tag{75}$$

$$C_4 = \psi_0 - \psi_1 - \frac{1}{EI_{ye2}}\left\{F_1\frac{(L_T+L_c)^2}{2}\right\} \tag{76}$$

By substituting Eq. 76 into Eq. 73, the general rotation profile for the second region is obtained as expressed in Eq. 77.

$$\frac{dw_2}{dz} = \frac{1}{EI_{ye2}}\left\{F_1\frac{z^2}{2}\right\} + \psi_0 - \psi_1 - \frac{1}{EI_{ye2}}\left\{F_1\frac{(L_T+L_c)^2}{2}\right\} \tag{77}$$

By integrating Eq. 77, the deformation profile for the second region is obtained as expressed in Eq. 78.

$$w_2 = \frac{1}{EI_{ye2}}\left\{F_1\frac{z^3}{6}\right\} + (\psi_0 - \psi_1)z - \frac{1}{EI_{ye2}}\left\{F_1\frac{(L_T+L_c)^2}{2}\right\}z + C_5 \tag{78}$$

Here, C_5 is the integration constant. Since the displacement at the hydrokinetic turbine level is known as a boundary condition, Eq. 79 can be written as the boundary condition.

Therefore, the deformation in the second section, w_2, is expressed as in Eq. 80.

$$\begin{aligned} w_2 = &\frac{1}{EI_{ye2}}\left\{F_1\frac{z^3}{6}\right\} + (\psi_0 - \psi_1)z - \\ &\frac{1}{EI_{ye2}}\left\{F_1\frac{(L_T+L_c)^2}{2}\right\}z + y_1 - \frac{1}{EI_{ye2}}\left\{F_1\frac{(L_T+L_c)^3}{6}\right\} - \\ &(\psi_0 - \psi_1)(L_T+L_c) + \frac{1}{EI_{ye2}}\left\{F_1\frac{(L_T+L_c)^2}{2}\right\}(L_T+L_c) \end{aligned} \tag{80}$$

The known displacement value at the wind turbine section determines the bending stiffness in the second section, EI_{ye2}, as expressed in Eq. 81.

$$\begin{aligned} &z = 0;\; w_2 = y_2 \\ &y_2 = y_1 - \frac{1}{EI_{ye2}}\left\{F_1\frac{(L_T+L_c)^3}{6}\right\} + (\psi_0 - \psi_1)(L_T+L_c) + \frac{1}{EI_{ye2}}\left\{F_1\frac{(L_T+L_c)^2}{2}\right\}(L_T+L_c) \end{aligned} \tag{81}$$

Therefore, the bending stiffness for the second section, EI_{ye2}, is determined using Eq. 82.

$$z = L_T + L_C;\ w_2 = y_1$$

$$EI_{ye2} = \frac{1}{y_1 - y_2 - (\psi_0 - \psi_1)(L_T + L_c)}\left\{F_1\frac{(L_T + L_c)^3}{6}\right\} + \frac{1}{y_2 - y_1 + (\psi_0 - \psi_1)(L_T + L_c)}\left\{F_1\frac{(L_T + L_c)^2}{2}\right\}(L_T + L_c) \tag{82}$$

In the first region, the maximum velocity occurs at the point where the maximum deformation occurs, which is the location of the applied force. The displacement at this point of force application can be expressed as in Eq. 83.

$$w_{2,m} = y_2 \tag{83}$$

Hence, the velocity profile can be expressed as in Eq. 84.

$$v = \frac{w_2}{w_{2,m}} v_{max} \tag{84}$$

The kinetic energy of a differential element in the second region, dT, can be expressed as in Eq. 85.

$$dT = \frac{1}{2}\rho A dz\left(\frac{w_2}{w_{2,m}} v_{max}\right)^2 \tag{85}$$

The kinetic energy of the second section is expressed using Eq. 86.

$$T_2 = \frac{1}{2}\int_0^{L_T+L_C} \rho A\left(\frac{w_2}{w_{2,m}} v_{max}\right)^2 dz$$
$$T_2 = \frac{1}{2}\rho A v_{max}{}^2 \frac{1}{w_{2,m}{}^2}\int_0^{L_T+L_C} (w_2)^2 dz \tag{86}$$

By dividing the numerator and denominator by the difference between the upper and lower integral limits, Eq. 86 transforms into Eq. 87.

$$T_2 = \frac{1}{2} m_{k2} \frac{v_{max}{}^2}{(L_T + L_C)} \frac{1}{w_{2,m}{}^2}\int_0^{L_T+L_C} (w_2)^2 dz \tag{87}$$

Here, m_{k2} is the mass of the second section and is given by Eq. 88.

$$m_{k2} = \rho A (L_T + L_C) \tag{88}$$

The coefficient for the effective mass is calculated using the expression in Eq. 89.

Table 2
Geometric Properties of the Combined Hybrid System [3,30].

Rotor nacelle assembly weight	m_{RNA}	350 t
Hydrokinetic turbine weight	m_{HYD}	120 t
Transition piece weight	m_{TRN}	172,8 t
Tower base diameter	D_b	3.87 m
Tower top diameter	D_r	6.00 m
Tower weight	m_T	347.46 t
Tower material density	ρ_T	8500 kg/m^3
Tower material elasticity modulus	E_T	210 GPa
Tower length	L_T	80 m
Distance between tower base and ground level	L_S	38 m
Distance between tower base and hydrokinetic turbine	L_C	24 m
Monopile diameter	D_P	6 m
Monopile wall thickness	t_P	70 mm
Monopile material elasticity modulus	E_P	210 GPa
Embedded monopile length	L_P	36 m
Monopile material density	ρ_P	7850 kg/m^3
Force acting on the hydrokinetic turbine	F_2	1.05 MN
Force acting on the wind turbine	F_1	0.79 MN

$$m_{eff2} = \left[\frac{1}{(L_T + L_C)}\frac{1}{y_2{}^2}\int_0^{L_T+L_C}(w_2)^2 dz\right] \tag{89}$$

Here, m_{eff2} is the effective mass coefficient for the second region. Consequently, in the natural frequency analysis, the mass in the second region, m_2, can be expressed using Eq. 90.

$$m_2 = m_{RNA} + m_{eff2} \times mk_2 \tag{90}$$

When writing the mass in the second region, m_2, if a transition is present, its mass should be included in this section. Considering soil effects, the spring constants are calculated using Eq. 91.

$$k_2 = \frac{F_2}{y_2 - y_1}$$
$$k_1 = \frac{F_1 + F_2}{y_1} \tag{91}$$

5. Verification and application of the model

For model verification, the study conducted by a group of researchers at Strathclyde University was considered [3]. This study utilized a 5 MW offshore wind turbine developed by the National Renewable Energy Laboratory (NREL). The dimensions and properties of the wind turbine, tower, and monopile were selected according to Phase 2 of the Offshore Code Comparison Collaboration (OC3) [30–31]. The 2 MW SeaGen system developed by Marine Current Turbines (MCT) was chosen as the hydrokinetic turbine.

A constant pile outer diameter of 6 m and a wall thickness of 70 mm were used for the monopile. The transition was included as an additional mass. Consequently, the monopile extends from the seabed to the foundation level of the tower. The wind turbine tower is identical to the one in OC3 Phase 2. The base and top of the tower are located 10 m and 90 m above the mean sea level, respectively. The tower's thickness and diameter taper linearly from the base to the top. The outer diameter and wall thickness at the tower's foundation and top were 6 m with 27 mm and 3.87 m with 19 mm, respectively.

Since the hydrokinetic turbines were assumed to operate synchronously, no torsional loads were expected and, therefore, were not considered. The loads from the hydrokinetic turbine were directly applied to the monopile. A simplified support structure was used to determine the drag forces acting on the structure [3]. These forces acting on this system were obtained from the thrust curves under the turbines' operating conditions. Subsequently, the system is modeled using ANSYS to calculate the natural frequency values.

The density of the soil layers varies from medium-dense to dense, and the rigidity of the layers increases with depth. In such stratified soils, as the rigidity of the deeper layers increases, the dynamic response contribution of the soil-structure interaction model is primarily governed by the upper layer. The lower layers ensure the appropriate overall foundation stiffness [32]. A similar conclusion was also drawn by [24], which stated that the layers closer to the surface play a more dominant role in displacement and stiffness calculations.

The natural frequency calculation for the combined hybrid system is carried out as follows:

I) In the first step, the geometric properties of the combined hybrid system are determined. The required geometric properties are taken from the verification study and provided in Table 2 [3].

I) The moment of inertia for the tower and the monopile is calculated by averaging the tower diameter and wall thickness using Eqs. 19 and 20.

$$D_T = 4.94\ m;\ t_T = 0.03\ m$$

Table 3
Comparison of the proposed method with the verification model for the system's natural frequency.

Proposed Method in Study	[3]	Difference (%)
0.213 Hz	0.218 Hz	2.35

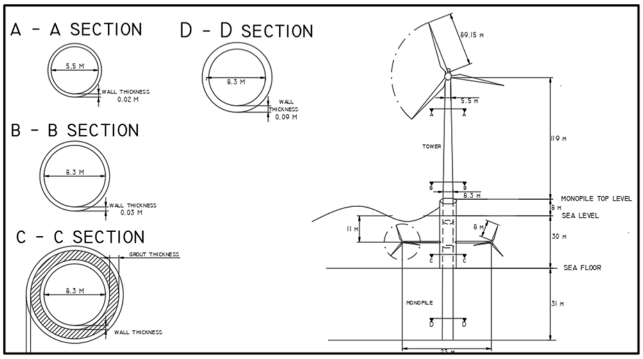

Fig. 6. Preliminary design of the combined hybrid system [6].

The moment of inertia for the tower and the monopile is calculated using Eqs. 17 and 18.

$I_T = 1.83\ m^4;\ I_P = 5.73\ m^4$

I) The flexibility coefficients of the soil springs are determined based on the soil properties. For this purpose, the subgrade reaction coefficient value is obtained from Table 1. In a study conducted by [32], the relative density of the soil under similar conditions was calculated as 55 % and classified as medium-dense sand. The validation study described the soil as cohesionless (sand), medium-dense, and located below the groundwater level. Therefore, the subgrade reaction coefficient was taken as 4848 kN/m³ from Table 1. An assessment using Eq. 29 determined that the pile is rigid in cohesionless soils. Accordingly, the flexibility coefficients of the soil springs are obtained as follows.

$$\delta_L = 2.8E-09\ kN/m^2$$

$$\delta_R = 4.4E-12\ kN/m^2$$

$$\delta_{LR} = 1.1E-10\ kN/m^2$$

II) The displacement and rotation values at the ground level are obtained from Eqs. 44 and 45.

$$y_0 = 0,017\ m;\ \psi_0 = 0,000665\ rad$$

III) The bending stiffness of the first and second sections is calculated using Eqs. 61 and 80.

$$EI_{ye1} = EI_{e1} = 2,83E11\ Nm^2;\ EI_{ye2} = EI_{e2} = 4,36E11\ Nm^2$$

IV) The rotation of the hydrokinetic turbine, ψ_1, is obtained from Eq. 52.

$$\psi_1 = 0,005279\ rad$$

Table 4
Geometric properties of the combined hybrid system [6].

Rotor nacelle assembly weight	m_{RNA}	679.85 t
Hydrokinetic turbine weight	m_{HYD}	300 t
Tower top diameter	D_t	5.50 m
Tower base diameter	D_b	8.30 m
Tower weight	m_T	673.65 t
Tower material density	ρ_T	8500 kg/m³
Tower material elasticity modulus	E_T	210 GPa
Tower length	L_T	115.63 m
Distance between tower base and ground level	L_S	38.19 m
Distance between tower base and hydrokinetic turbine	L_C	24 m
Monopile diameter	D_P	8.3 m
Monopile wall thickness	t_P	100 mm
Monopile material elasticity modulus	E_P	210 GPa
Embedded monopile length	L_P	31 m
Monopile material density	ρ_P	7850 kg/m³
Force acting on the hydrokinetic turbine	F_2	2.19 MN
Force acting on the wind turbine	F_1	1.50 MN

Table 5
The natural frequency of the structure with only the DTU 10 MW reference wind turbine.

Research	Proposed method	Simis Ashes	Difference (%)
[35]	0.179 Hz	0.183 Hz	2.23

Table 6
Comparison of the natural frequency of the structures.

Frequency of Offshore Wind Turbine	Frequency of Combined Hybrid System	Reduction (%)
0.179 Hz	0.135 Hz	24.59

V) The deformation caused by the applied forces at the force application points is determined using Castigliano's theorem and calculated through Eqs. 15 and 16.

$$q_1 = \frac{\partial U}{\partial F_1} = 0.566\ m;\ q_2 = \frac{\partial U}{\partial F_2} = 0.008\ m$$

VI) The deformation at the hydrokinetic turbine level, y_1, and the deformation at the wind turbine level, y_2, are calculated.

$$y_1 = 0.034\ m;\ y_2 = 1.136\ m$$

VII) The spring constants for the first and second sections are calculated as follows.

$$k_2 = \frac{F_2}{y_2 - y_1} = 954866\ N/m$$

$$k_1 = \frac{F_1 + F_2}{y_1} = 54554697\ N/m$$

VIII) The effective mass coefficients are calculated using Eqs. 69 and 87.

$$m_{eff1} = 0.228;\ m_{eff2} = 0.280$$

IX) The masses in the first region, m_1, and the second region, m_2, are calculated as follows.

Table 7
Lower and upper operating frequencies of turbines in the combined hybrid system.

Lower rotor speed			Upper rotor speed		
Wind Turbine (DTU 10 MW)					
Speed (rpm)	Frequency 1P (Hz)	Frequency 3P (Hz)	Speed (rpm)	Frequency 1P (Hz)	Frequency 3P (Hz)
6	0.1000	0.3000	9.6	0.1600	0.4800
Hydrokinetic Turbine (SeaGen 1.2 MW)					
4	0.0667	0.2000	11.5	0.1917	0.5750

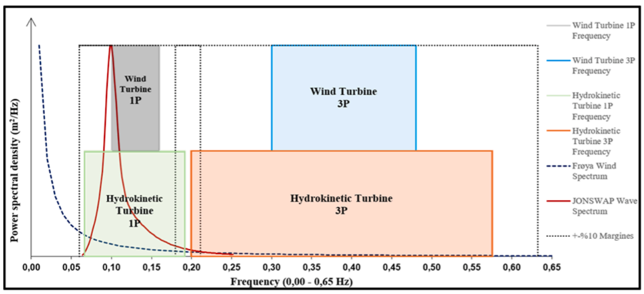

Fig. 7. Operating frequencies of the turbines.

$$m_1 = m_{HYD} + m_{eff1} \times mk_1 = 134691\ t$$

$$m_2 = m_{RNA} + m_{eff2} \times mk_2 = 526485\ t$$

The system's natural frequency is calculated using Eq. 91, completing the analysis.

$f_1 = 0.213\ Hz$

In the validation model, three different monopile wall thickness values were analyzed. The results obtained using the developed model have been compared with those from [3] in Table 3.

As seen in Table 3, the difference between the value obtained from the proposed method and the result reported in the literature is 2.35 %, indicating good agreement and supporting the consistency of the model. Although only one reference was available for direct comparison, this deviation is within the accepted tolerance range for frequency-domain analytical models. Furthermore, broader validation could not be performed due to the limited availability of studies on hybrid offshore wind–hydrokinetic systems with similar configurations. Future work may consider additional verification using experimental data or high-fidelity numerical simulations involving coupled fluid–structure interaction.

5.1. Case study: Türkiye/Kırklareli Kıyıköy

In this section, the natural frequency analysis of the combined hybrid system will be conducted for the Kırklareli Kıyıköy region in Türkiye. The preliminary design of the combined hybrid system for this region, as previously studied by [6], is presented in Fig. 6.

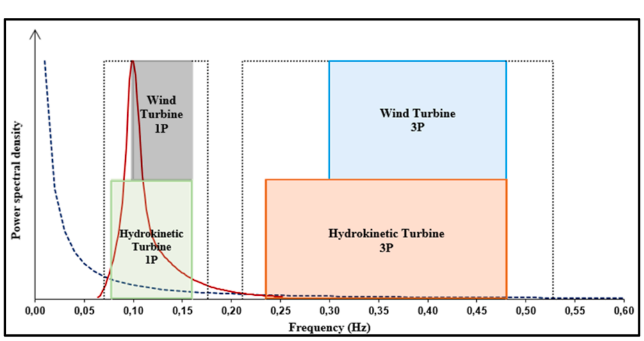

Fig. 8. Revised turbine frequencies.

In [6], the DTU 10 MW reference wind turbine [33] was used as the wind turbine, while the SeaGen 1.2 MW [34] hydrokinetic turbine was selected as the source of current energy. Based on soil borehole logs, the soil in the Kıyıköy region was classified as medium-dense sand. The geometric properties of the combined hybrid system, as shown in Fig. 6, are presented in Table 4 [6].

If the system provided by [6] includes only the wind turbine, the natural frequency value can be determined using the method provided by [35] and obtained from Simis Ashes, which is a commonly used wind turbine design and analysis software [36]. The findings are presented in Table 5.

Thus, in the case of only a wind turbine, the natural frequency was calculated as 0.179 Hz [35]. Following the calculation steps outlined, the natural frequency of the new combined hybrid system (including both the wind and hydrokinetic turbines), as shown in Fig. 6, was calculated as 0.135 Hz (Table 6).

As seen in Table 6, the natural frequency of the combined hybrid system decreases by 24.59 % compared to the case with only the wind turbine. This drop in frequency necessitated significant structural redesign, the details of which are presented in next section. The critical excitation frequency ranges for both turbines are summarized in Table 7.

In Table 7, the upper row represents the operating frequency range of the DTU 10 MW wind turbine, and the lower row corresponds to the operating frequency range of the SeaGen 2 MW hydrokinetic turbine. The operating frequencies are graphically represented in Fig. 7.

As seen in Fig. 7, when a 10 % safety margin is added to the turbines' operating frequencies, the soft-stiff design region is eliminated. In this analysis, the Frøya wind spectrum, as proposed by [37], has been used as the wind spectrum model (Eq. 92).

$$S(f) = 320\left(\frac{U_{ref}}{10}\right)^2\left(\frac{z}{10}\right)^{0,45}(1+X^n)^{-5/3n}$$
$$X = 172\left(\frac{U_{ref}}{10}\right)^{-0,75}\left(\frac{z}{10}\right)^{2/3}f;\ n = 0.468 \tag{92}$$

Here, S(f) is the wind spectrum value, U_{ref} is the wind speed measured at a reference height of 10 m above sea level, z is the height at which the wind speed is measured, X is the length scale in dimensionless frequency, f is the frequency and n is a constant. The reference wind speed at 10 m for the Kıyıköy region was obtained using the HYDROTAM-3D software. HYDROTAM-3D is a three-dimensional hydrodynamic and transport model validated against analytical and experimental results published in scientific sources and field studies. It has been applied to various coastal areas in Turkey [38–39]. In Fig. 7, the JONSWAP wave spectrum has been used as the wave spectrum model [40] (Eq. 93).

$$S(\omega) = \frac{\alpha g^2}{\omega} exp\left(-\frac{5\omega_p^4}{4\omega^4}\right)^2 \gamma^r;\ \alpha = 0,0081,\ \gamma = 3.3$$
$$r = exp\left[-\frac{(\omega-\omega_p)^2}{2\sigma^2\omega_p^2}\right] \tag{93}$$
$$\sigma = 0,07(\omega < \omega_p);\ \sigma = 0,09(\omega \geq \omega_p);$$

Table 8
Revised lower and upper operating frequencies of turbines in the combined hybrid system.

Lower rotor speed			Upper rotor speed		
Wind Turbine (DTU 10 MW)					
Speed (rpm)	Frequency 1P (Hz)	Frequency 3P (Hz)	Speed (rpm)	Frequency 1P (Hz)	Frequency 3P (Hz)
6	0.1000	0.3000	9.6	0.1600	0.4800
Hydrokinetic Turbine (SeaGen 1.2 MW)					
4.7	0.0783	0.2350	9.6	0.1600	0.4800

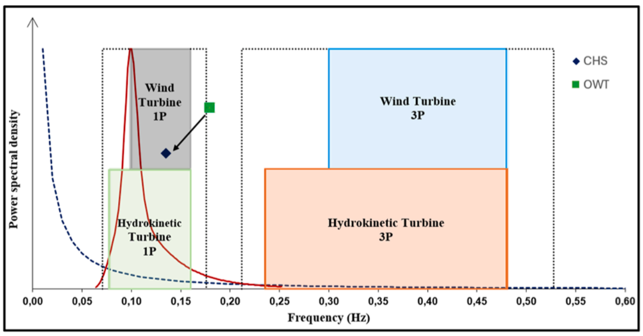

Fig. 9. Revised turbine frequencies and natural frequencies of the structures.

Table 9
Structural Component Adjustments for the Optimized Hybrid System.

	Original Value	Optimized Value	Increase
Tower base wall thickness	0.038 m	0.080 m	%57.9
Tower mass	673.65 t	895.73 t	% 32.97
Monopile wall thickness	90 mm	150 mm	% 66.67
Monopile embedded length	31,00 m	54.00 m	% 74.19
Monopile mass	558.83 t	1247.47 t	%123.23
Frequency	0.135 Hz	0.179 Hz	%24.59

Here, $S(\omega)$ is the wave spectrum value, α is the shape parameter, g is the gravitational acceleration, ω is the wave frequency, ω_p is the peak wave frequency, and γ is the peak correction factor.

Since the soft-stiff region has vanished, the operating frequencies of the hydrokinetic turbine have been adjusted to restore the frequency limits to those of the wind turbine-only case (Fig. 8).

As seen in Fig. 8, the soft-stiff design region has been restored by increasing the lower operating speeds and decreasing the higher operating speeds of the hydrokinetic turbine. The revised lower and upper operating frequencies of the turbines are presented in Table 8

As seen in Table 8, the soft-stiff region has been expanded by reducing the hydrokinetic turbine's lower and upper operating speeds. The natural frequencies of the offshore wind turbine and the combined hybrid system, as presented in Table 8, are illustrated in Fig. 9.

In Fig. 9, the green square represents the Wind Turbine Only (WTO) system, while the blue diamond represents the Combined Hybrid System (CHS). As seen in Fig. 9, when only the wind turbine is present, the design falls within the soft-stiff region. However, when the combined hybrid system is considered, the structure's natural frequency shifts into the resonance zone. This shift indicates that solving the system with a second-degree-of-freedom approach causes the natural frequency to move from the soft-stiff region into the resonance region. This finding suggests that the design initially considered safe under a first-degree-of-freedom solution becomes unsafe when a second-degree-of-freedom analysis is applied.

6. Structural optimization to restore natural frequency

The significant structural modifications applied to address the frequency drop discussed in earlier sections are detailed in this dedicated section to guide the reader toward the applied optimization strategy. These changes aim to demonstrate how the hybrid system was adapted to recover dynamic performance under soil-interactive conditions.

This 24.59 % reduction in natural frequency highlights a significant shift in the system's dynamic behavior and raises important engineering concerns. In particular, bringing the natural frequency closer to environmental excitation bands, such as wave loading and turbine harmonics (e.g., 1P/3P), can increase the resonance and dynamic amplification risk.

In our specific case, the frequency reduction necessitated considerable structural changes, including increased foundation depth and wall thickness, which can be considered a partial redesign. Not all hybrid systems require such redesign; the need arises particularly when site-specific soil conditions and dynamic interactions lead to substantial shifts in natural frequency. However, this does not imply that hybrid systems are inherently unfeasible. Rather, it demonstrates that such systems require a more integrated and iterative design process that explicitly incorporates soil structure interaction and dynamic coupling effects from the outset. Structural optimization strategies such as stiffness enhancement and mass redistribution remain effective tools to restore dynamic performance but must be applied early and site-specifically.

A geometry-based structural optimization was performed to restore the natural frequency to the optimal design range in the hybrid system with soil–structure interaction. The modifications focused on enhancing global stiffness and controlling mass distribution. Key parameters such as the tower base wall thickness, monopile wall thickness, monopile embedded length, and total mass were incrementally adjusted using a trial-and-error process. These engineering decisions were based on dynamic sensitivity and practical feasibility.

The optimized values and their corresponding percentage increases are summarized in Table 9.

As a result of these structural adjustments, the first natural frequency of the system increased from 0.135 Hz (pre-optimization) to 0.179 Hz (post-optimization), placing it safely outside the combined 1P/3P excitation bands of both turbines.

These adjustments collectively restored the natural frequency to a range that avoids overlap with critical excitation sources such as wave frequencies or operational harmonics (1P, 3P). This highlights the importance of explicitly incorporating foundation stiffness and soil interaction in hybrid system design. However, it must also be acknowledged that the 54-meter pile depth exceeds the verified soil profile in the site-specific borehole data, which ends at 23 m Further geotechnical exploration would be required to verify whether competent strata or rock exists at the new embedded depth.

This case demonstrates that frequency shifts introduced by soil flexibility in hybrid systems are not design-fatal. Rather, they present an opportunity for optimization that enables safe and efficient operation through rational structural modifications aligned with site-specific constraints.

7. Results

The analytical model introduced in the study was validated by comparing its results with those from a reference study conducted by researchers at the University of Strathclyde. Using parameters from the

OC3 Phase 2 design and the SeaGen hydrokinetic turbine system, the natural frequency of the hybrid offshore structure was calculated. The proposed method estimated a natural frequency of 0.213 Hz, which differed by only 2.35 % from the 0.218 Hz value obtained in the reference model, confirming the accuracy of the simple analytical approach. This level of agreement highlights the potential of the presented multi-degree-of-freedom (MDOF) framework to replace more time-intensive finite element models in early-stage design phases for combined offshore energy systems.

The analytical model was then applied to a case study situated in Kırklareli Kıyıköy, Türkiye. Using the DTU 10 MW wind turbine and SeaGen 1.2 MW hydrokinetic turbine configurations, the natural frequency of the combined hybrid system was computed as 0.135 Hz. This value represents a 24.59 % decrease from the 0.179 Hz calculated for the wind turbine-only configuration, highlighting the critical influence of additional hydrokinetic mass and stiffness properties. The significant frequency drop indicated that systems previously deemed structurally safe under a single-degree-of-freedom approach might fall into resonance zones when modeled as a second-degree system, underlining the need for more complex hybrid design modeling.

The operational frequency ranges of both the wind and hydrokinetic turbines were analyzed. It was shown that, due to the downward shift in natural frequency caused by combining systems, the safe "soft-stiff" design region effectively disappears unless turbine operational speeds are adjusted. By narrowing the operating frequency range of the hydrokinetic turbine, the study successfully restored the soft-stiff region, which is critical for avoiding resonance. Graphical results indicated that while the wind-only system remained in the safe design region, the hybrid system initially fell into the resonance zone, suggesting a need for revised turbine specifications or structural stiffening. These results emphasize the importance of frequency-tuned design and operating range optimization in hybrid offshore renewable energy systems.

8. Discussions

The HCTs are added to monopile foundation of hybrid systems with local stiffening at the attachment level as demonstrated in recent engineering applications:

1) Transition-piece jackets and clamp collars: [4] designed a 6 m-diameter, 60 m-long monopile with a 29 m transition sleeve at the Cook Strait between the North and South Islands of New Zealand. The monopile supported the wind-hydrokinetic hybrid system with two HCTs in shallow water. These pods were bolted through the sleeve so that the extra torque was carried locally by a thicker (83 mm) shell and internal stiffener rings, leaving the main pile thickness unchanged.
2) Braced collars and tripod outriggers: [41] analyzed the Cook Strait hybrid system with one wind and two HCTs by welding three short braces to the pile at –25 m MSL, and they restricted tip deflection to code limits without changing the 6 m × 0.083 m wall section. The Atlantic Resources AR 2000 current turbine was used with a Siemens SWT-3.6–107 wind turbine for the hybrid system.
3) Monopile + Plate (HOREHS) System: [42] established a hybrid offshore renewable energy harvest system (HOREHS) on a shared platform for the wind energy harvested by the offshore wind turbine (OWT), the wave energy harvested by the wave energy converter (WEC), and the hydrokinetic energy collected by the HCT to reduce energy costs and increase production. The HOREHS system at the Sheringham Shoal site was supported by a fixed foundation and consisted of a monopile and a steel plate.
4) [43] and [44] showed that integrating wind and hydrokinetic energy systems has been a feasible combination to solve the economic viability issue for energy. Two configurations were proposed by [45] and [46] for the wind-hydrokinetic hybrid system in deep water. The first configuration was integrating two HCTs to spar-buoy foundations, and the second was installing the HCT at the bottom of the semi-submersible foundation.

As a result, the frequency analysis model developed in this paper can be effectively used for large-scale engineering applications, because the added structural mass is concentrated within 10 m of the mudline, the bending stiffness and the first two eigenmodes change far more than predicted by a one-DOF tower-only model. High-fidelity FE solutions exist, but they are time-consuming. The practical attachment details fit within the two-DOF abstraction adopted, and the proposed closed-form frequency model has the potential for engineering realization due to its following advantages:

1. Rapid Application: The developed model enables early design iterations before costly FE or basin testing.
2. Parametric Optimization: Designers can sweep collar mass, plate radius, or turbine mass in seconds to keep the 1st natural frequency outside the now-narrow soft-stiff band.
3. Complementary Solutions: Detailed FE models (or soil–pile macro-elements) refine fatigue and ULS checks once a feasible design envelope is found.

The model can effectively be used in hybrid-monopile design studies, and its relevance will increase as larger (>15 MW) wind turbines narrow the admissible frequency frame further [47]

As a result, the structural integration is progressing from concept towards pilot-scale reality, and the simplified dynamic-analysis framework provides an essential, rapid screening model for such emerging designs.

9. Conclusions

This study presented the mechanisms and analytical equations while conducting the natural frequency analysis of second-degree-of-freedom combined hybrid systems. The accuracy of the proposed approach was validated by comparing it with existing literature, yielding a 2.35 % difference and confirming its reliability.

The natural frequency analysis was systematically outlined, which is crucial for the design of combined hybrid systems. One of the most critical aspects highlighted in this study is that an adaptive approach was introduced, unlike the fixed effective mass coefficients used in the literature. The study summarizes how these coefficients are determined based on the resulting deformations, ensuring a more accurate and dynamic evaluation in natural frequency analysis.

When considering the natural frequency in the design of combined hybrid systems, evaluating the system based on a second-degree-of-freedom approach rather than a first-degree-of-freedom approach has resulted in a 24.59 % reduction in the natural frequency value.

In the first-degree-of-freedom solution of the combined hybrid system examined in this study, the structure was found to be safe, according to [24]. However, in the second-degree-of-freedom solution, the structure falls into an unsafe region, highlighting the importance of considering higher-order dynamics in the design process. Furthermore, the applicability and limitations of the model have been explicitly discussed. The proposed model validates symmetric, single-turbine configurations with aligned environmental loading. Although it does not currently cover asymmetric layouts or multi-turbine systems, it can be extended to such configurations by incorporating additional degrees of freedom and more complex dynamic coupling. This clarification ensures that the modeling remains physically consistent with the system geometry and avoids oversimplifications in some SDOF-based approaches, such as in [4].

In addition to structural redesign, an operational adjustment strategy was implemented to recover the dynamic safety margin. Specifically, the rotor speed range of the hydrokinetic turbine (SeaGen 1.2 MW) was revised from 4–11.5 rpm to 4.7–9.6 rpm. This frequency tuning was achieved without modifying the rotor geometry. Instead, the adjustment was made through system-level regulation and generator control, allowing the hydrokinetic turbine's excitation frequencies (1P and 3P) to be shifted away from resonance zones. This approach demonstrates that non-invasive operational tuning can mitigate certain resonance risks, providing a flexible method for early-stage hybrid system integration.

As a recommendation for future studies, it is suggested that the hydro-damping effect, which varies with depth, should be incorporated dynamically into the natural frequency analysis of the structure. Although the current study is focused on fixed-bottom hybrid systems, the two-degree-of-freedom analytical framework and frequency-domain modeling approach developed here may serve as a conceptual and methodological basis for floating offshore wind turbines (FOWTs) [48], especially under seismic and multi-hazard conditions. Unlike traditional time-domain simulations, frequency-based models allow for rapid evaluation of resonance risks and parametric sensitivity, which are particularly relevant aspects for early-stage FOWT design. However, the present model does not yet incorporate platform pitch–roll dynamics or mooring system flexibility, which are critical in floating configurations.

Recent studies support this direction: [49] demonstrated that vertical seabed acceleration from seaquakes can induce nacelle accelerations exceeding 0.3 g, even in tension-leg configurations [50] emphasized the impact of fluid compressibility and seabed energy absorption on vertical responses using coupled fluid–structure interaction models [51] long-period multidirectional ground motions trigger amplified platform responses, particularly in semi-submersibles. These studies reveal that seismic effects on FOWTs are tightly linked to structural resonance and damping — themes directly addressed in the present framework. Future work could extend this 2DOF formulation by incorporating pitch, heave, surge motions, and mooring dynamics, creating a frequency-domain toolkit for early-phase seismic safety screening of floating hybrid platforms. Based on these findings, this study is expected to serve as a milestone and guide for future combined hybrid system designs.

CRediT authorship contribution statement

Abdullah Kürşat DEMİR: Investigation, Formal analysis, Methodology, Software, Validation, Visualization, Writing – review & editing. **Can Elmar BALAS:** Supervision, Project administration, Resources, Writing – review & editing.

Declaration of competing interest

None

Data availability

Data will be made available on request.

References

[1] R. Samso, J. Crespin, A. Garcia–Olivares, J. Sole, Examining the potential of marine renewable energy: A net energy perspective, Sustainability 15 (2023) 8050, https://doi.org/10.3390/su15108050.

[2] B. Önöz, Wave Energy, Presented at the Clean Energy Days, Istanbul Technical University, Istanbul, 2013.

[3] HoWAT. https://www.esru.strath.ac.uk/EandE/Web_sites/16-17/WindAndTidal/ (accessed 30 August 2024).

[4] N.M. Nasab, J. Kilby, L. Bakhtiaryfard, Analysis and design of monopile foundations for offshore wind and tidal turbine structures, Water (Basel) 14 (2022) 3555, https://doi.org/10.3390/w14213555.

[5] L. Cui, S. Amani, M. Gabr, W.G.P. Kumari, W.G. P, A. Ahmed, H. Ozcan, B.A. Horri, S. Bhattacharya, Synergistic Hybrid Marine renewable energy Harvest System, Energies (Basel) 17 (2024) 1240, https://doi.org/10.3390/en17051240.

[6] A.K. Demir, C.E. Balas, L. Balas, Enhancing Türkiye's renewable energy capacity: an advanced hybrid model for combined offshore wind and wave turbines design utilizing Hydrodynamic and Monte Carlo Simulations, J. Coast. Res. 113 (2024) 793–798, https://doi.org/10.2112/JCR-SI113-156.1.

[7] Q. Hassan, S. Algburi, A.Z. Sameen, H.M. Salman, M. Jaszczur, A review of hybrid renewable energy systems: solar and wind-powered solutions – Challenges, opportunities, and policy implications, Results Eng. 20 (2023) 101621, https://doi.org/10.1016/j.rineng.2023.101621.

[8] K.P. Kumar, D.C. Das, N. Soren, A.S. Veerendra, A. Flah, A. Alkuhayli, R. Ullah, A multi-energy inertia-based coordinated voltage and frequency regulation in isolated hybrid power system using PI-TISMC, J. Energy Storage 77 (2024) 109637, https://doi.org/10.1016/j.est.2024.109637.

[9] B. Shahulhameed, A.S. Gopinath, E.K. Jishor, R. Thangavelu, K.K. Koyyala, R. K. Dilba, Feasibility analysis of green hydrogen generation from offshore energy resources, In: M.R. Phillips, S. Al–Naemi, C.M. Duarte (Eds), *Coastlines under Global Change: Proceedings from the International Coastal Symposium (ICS) 2024 (Doha, Qatar)*, J. Coast. Res. (113) (2024) 971–975, https://doi.org/10.2112/SI113-195.1. Special Issue No..

[10] A. Kechida, D. Gozim, B. Toual, M.M. Alharthi, T.F. Agajie, S.M.S. Ghoneim, R.N. R. Ghaly, Smart control and management for a renewable energy based stand-alone hybrid system, Sci. Rep. 14 (2024) 32039, https://doi.org/10.1038/s41598-024-32039-7. Article No.

[11] T.M. Alabi, L. Lu, Z. Yang, Real-time automatic control of multi-energy system for smart district community: a coupling ensemble prediction model and safe deep reinforcement learning, Energy 304 (C) (2024), https://doi.org/10.1016/j.energy.2024.127701.

[12] A. Johri, V. Verma, M. Basu, Optimization and intelligent control in hybrid renewable energy systems incorporating solar and biomass, Energy Eng. 122 (5) (2025) 1887–1918, https://doi.org/10.32604/ee.2025.062355.

[13] ESMAP, Going global: expanding offshore wind to emerging market. Energy Sector Management Assistance Program, 2020.

[14] A. Davison, T. Mallows, Strangford Lough Marine Current Turbine Environmental Statement (Non-Technical Summary), Royal Haskoning Ltd, Edinburg, 2005. Project No. 9P5161.

[15] S. Bhattacharya, Challenges in design of foundations for offshore wind turbines, Eng. Technol. Ref. (2014) 1, https://doi.org/10.1049/etr.2014.0041.

[16] L. Arany, S. Bhattacharya, J.H.G. MacDonald, S.J. Hogan, Closed-form solution of eigen frequency of monopile supported offshore wind turbines in deeper waters incorporating stiffness of substructure and SSI, Soil Dyna. Earthq. Eng. 83 (2016) 18–32, https://doi.org/10.1016/j.soildyn.2015.12.011.

[17] I.B. Loken, Dynamic Response and Fatigue of Offshore Wind Turbines - Effect of Foundation Type and Modelling Method Using Software FAST, Norwegian University of Science and Technology Faculty of Engineering Department of Structural Engineering, Trondheim, 2017. Master of Science Thesis.

[18] P. Alkhoury, A – H. Soubra, V. Rey, M. Ait–Ahmed, A full three-dimensional model for the estimation of the natural frequencies of an offshore wind turbine in sand, Wind Energy 24 (2020) 699–719, https://doi.org/10.1002/we.2598.

[19] D. Amel, A.B. Djillali, S. Bhattacharya, A. Nasreddine, Evaluation of sand p–y curves by predicting both monopile lateral response and OWT natural frequency, Studia Geotechnica et Mechanica 44 (2022) 66–81, https://doi.org/10.2478/sgem-2022-0003.

[20] Y. Jiang, X. Zhou, Y. Liu, Simplified calculation method for the natural frequencies of the offshore wind turbine structures with monopile foundations based on Euler–Bernoulli Beam theory, Adv. Civil Eng. (2023) 8262901, https://doi.org/10.1155/2023/8262901. Article ID.

[21] I. Diaz, Offshore Wind and Tidal Stream Plant, Escola Tecnica Superior d'Enginyeria Industrial de Barcelona, 2019. Master's Thesis.

[22] DNV, Offshore Standard Det Norske Veritas DNV– Os – J101, Design of Offshore Wind Turbine Structures, Det Norske Veritas, 2014.

[23] J. Jonkman, W. Musial, Offshore Code Comparison Collaboration (OC3) For IEA Task 23 Offshore Wind Technology and Deployment, National Renewable Energy Laboratory, 2010. NREL/TP-500-48191.

[24] L. Arany, S. Bhattacharya, J.H.G. MacDonald, S.J. Hogan, Design of monopiles for offshore wind turbines in 10 steps, Soil Dyna. Earthq. Eng. 92 (2017) 126–152, https://doi.org/10.1016/j.soildyn.2016.09.024.

[25] W. Shaofeng, T.J. Larsen, H. Bredmose, Ultimate load analysis of a 10 MW offshore monopile wind turbine incorporating fully nonlinear irregular wave kinematics, Marine Struct. 76 (2020) 102922, https://doi.org/10.1016/j.marstruc.2020.102922 (2021).

[26] H.G. Poulos, E.H. Davis, Pile Found. Analy. Des. (1980).

[27] K. Terzaghi, Evaluation of coefficients of subgrade reaction, Géotechnique 5 (1955) 297–326, https://doi.org/10.1680/geot.1955.5.4.297.

[28] A. Vesic, Bending of beams resting on isotropic elastic solid, J. Eng. Mech. Divis. 87 (1961) 35–53, https://doi.org/10.1061/JMCEA3.0000212.

[29] S. Timoshenko, Vibration Problems in Engineering, second ed, D. Van Nostrad Company, New York, 1937.

[30] J. Jonkman, S. Butterfield, W. Musial, G. Scott, Definition of a 5-MW reference wind turbine for offshore system development, Technical Report, NREL/TP –500 –38060, 2009.

[31] J. Jonkman, Definition of the floating system for phase IV of OC3, Technical Report, NREL/TP –500 –47535, 2010.

[32] P. Passon, OC3 memo from SWE, memorandum: derivation and description of the soil-PileInteraction models, IEA – Annex XXIII Subtask, 2006.

[33] C. Bak, F. Zahle, R. Bitsche, T. Kim, A. Yde, L.C. Henriksen, M.H. Hansen, J.P.A. Blasques, M. Gaunaa,A. Natarajan, The DTU 10-MW reference wind turbine, 2013.

[34] A.K. Demir, Development of an Optimal Offshore Combined Wind and Blue Energy Plant for Türkiye, Gazi University, 2025. PhD Thesis.

[35] Wind turbine design with superpowers. https://www.simis.io/#products, 2024 (accessed 29 August 2024).

[36] O.J. Andersen, J. Lovseth, The Frøya database and maritime boundary layer wind description, Marine Struct. 19 (2006) 173–192, https://doi.org/10.1016/j.marstruc.2006.07.003.
[37] L. Balas, E. Özhan, A baroclinic three dimensional numerical model applied to coastal lagoons, Comput. Sci. —ICCS 2003 2658 (2003) 205–212, https://doi.org/10.1007/3-540-44862-4_23.
[38] E.A. Balas, A. Uğurlu, C.E. Balas, A hybrid probabilistic design model of riverine jetties incorporating three-dimensional numerical simulations of transport phenomena in the context of emerging climate change, J. Coast. Res. 113 (2024) 220–224, https://doi.org/10.2112/JCR-SI113-044.1.
[39] K. Hasselmann, D.B. Ross, P. Muller, W. Sell, A parametric wave prediction model, J. Phys. Oceanogr. 6 (1976) 200–228, https://doi.org/10.1175/1520-0485(1976)006≤0200:APWPM≥2.0.CO;2.
[40] N.M. Nasab, A. Wang, Minimizing the displacement of integrated system of wind and tidal turbines based on the soil types under cyclic loads, AIMS Geosci. 9 (3) (2023) 513–527, https://doi.org/10.3934/geosci.2023028.
[41] Y. Ma, L. Cui, S. Bhattacharya, A novel foundation design for the hybrid offshore renewable energy harvest system, Ocean Eng. 323 (2025) 120519, https://doi.org/10.1016/j.oceaneng.2025.120519.
[42] D. Lande-Sudall, T. Stallard, P. Stansby, Co-located offshore wind and tidal stream turbines: assessment of energy yield and loading, Renew. Energy 118 (2018) 627–643, https://doi.org/10.1016/j.renene.2017.10.063.
[43] D. Lande-Sudall, T. Stallard, P. Stansby, Co-located deployment of offshore wind turbines with tidal stream turbine arrays for improved cost of electricity generation, Renew. Sustain. Energy Rev. 104 (2019) 492–503, https://doi.org/10.1016/j.rser.2019.01.035.
[44] Y. Yang, J. Fu, Z. Shi, L. Ma, J. Yu, F. Fang, S. Chen, Z. Lin, C. Li, Performance and fatigue analysis of an integrated floating wind-current energy system considering the aero-hydro-servo-elastic coupling effects, Renew. Energy 216 (2023) 119111, https://doi.org/10.1016/j.renene.2023.119111.
[45] Y. Yang, Z. Shi, J. Fu, L. Ma, J. Yu, F. Fang, C. Li, S. Chen, W. Yang, Effects of tidal turbine number on the performance of a 10 MW-class semi-submersible integrated floating wind-current system, Energy 285 (2023) 128789, https://doi.org/10.1016/j.energy.2023.128789.
[46] J.L. Wilk-Jakubowski, L. Pawlik, G. Wilk-Jakubowski, R. Harabin, State-of-the-art in the use of renewable energy sources on the example of wind, wave energy, tidal energy, and energy harvesting: A review from 2015 to 2024, Energies (Basel) 18 (6) (2025) 1356, https://doi.org/10.3390/en18061356.
[47] A.A.T. Alkhalidi, H.A. Kaylani, N. Alawawdeh, Technology assessment of offshore wind turbines: floating platforms – Validated by case study, Results Eng. 17 (4) (2022) 100831, https://doi.org/10.1016/j.rineng.2022.100831.
[48] A.M. Kaynia, H. Blekastad, P. Schell, E.L. Walter, Seismic response of floating wind turbines due to seaquakes, Wind Energy 26 (2) (2023) 145–162, https://doi.org/10.1002/we.2791.
[49] J.H. Lee, J.K. Kim, Dynamic response analysis of a floating offshore structure subjected to the hydrodynamic pressures induced from seaquakes, Ocean Eng. 101 (2015) 25–39, https://doi.org/10.1016/j.oceaneng.2015.04.010.
[50] W. Yu, P. Wang, M. Zhao, R. Xi, X. Du, A numerical method for evaluating the earthquake response of a 5 MW OC4 semi-submersible FOWT under multidirectional excitations, Soil Dyna. Earthq. Eng. 196 (2025) 109467, https://doi.org/10.1016/j.soildyn.2025.109467.